Realizing efficient photocatalytic water splitting over Mg-modified BaNbO$_2$N under visible light illumination

Lin Yang [a,b], Zhuo Li [c], Xiaoxiang Xu [a,b,*]

[a] Clinical and Central Lab, Putuo People's Hospital, Tongji University, Shanghai 200060, China
[b] Shanghai Key Lab of Chemical Assessment and Sustainability, School of Chemical Science and Engineering, Tongji University, Shanghai 200092, China
[c] College of Environment Science and Engineering, Tongji University, Shanghai 200092, China

ARTICLE INFO

ABSTRACT

With a light absorption up to 740 nm, BaNbO$_2$N is promising for solar water splitting but normally owns a low activity due to a high defect concentration. Here, Mg is adopted as a dopant to modify the BaNbO$_2$N. The presence of Mg not only reduces the defect concentration and enhances surface hydrophilicity but also tunes the bandgap as well as the band edge positions. These modifications greatly promote the charge separation and transfer of BaNbO$_2$N, boosting the photocatalytic activities for O$_2$-evolution reactions. An apparent quantum efficiency of 1.65 % at 420 $\pm$ 20 nm has been attained for Mg modified BaNbO$_2$N. Overall water splitting at a stable gas-evolution rate ($\sim$ 2.0 μmol·h^{-1} for H$_2$ and $\sim$ 1.0 μmol·h^{-1} for O$_2$) has been realized by integrating Mg-modified BaNbO$_2$N into a Z-scheme system. These findings justify Mg as an effective dopant to modulate the photocatalytic behavior of Nb-based perovskite oxynitrides.

1. Introduction

Perovskite oxynitrides, *i.e.*, AM(O,N)$_3$ (A = Ca, Sr, Ba, and La *etc.*; M = Ti, Nb, and Ta *etc.*) have gained considerable research interests as water splitting photocatalysts not only because of their strong visible light absorption but also due to their suitable band edge alignments relative to water redox potentials [1–6]. Since visible light photons account for $\sim$ 47 % of the solar spectrum, perovskite oxynitrides are capable of harvesting considerable amounts of solar photons for photocatalytic reactions as opposed to the wide-bandgap semiconductor counterparts [7–11].

This is typically true for Nb-based perovskite oxynitrides which have almost the narrowest bandgap among perovskite oxynitrides [12–16]. For instance, BaNbO$_2$N has a bandgap of $\sim$ 1.7 eV and can strongly absorbs visible photons as far as 740 nm [17]. Nevertheless, the photocatalytic activity of BaNbO$_2$N and other Nb-based perovskite oxynitrides is generally very poor under ordinary conditions, being quite incompatible with their extraordinary light absorption capability [18, 19]. This has been attributed to the high defect concentration of Nb-based perovskite oxynitrides that undergo severe defect-induced photocarrier recombination rather than photocatalytic reactions. These defects are intrinsically formed during current synthetic

procedures which involve high-temperature ammonolysis treatment. For instance, Nb^{5+} has a relatively high electronegativity thereby is prone to form reduced Nb species (*e.g.* Nb^{4+} and Nb^{3+}) in the presence of hot ammonia gas [20,21]. In this regard, controlling the defect concentration is the key to open up the photocatalytic potential of Nb-based perovskite oxynitrides.

Previous studies have shown that doping alkaline or alkaline earth cations is helpful to reduce the defect concentration [22–26]. These cations are of low electronegativity thereby can stabilize the high-valence transition cations (*e.g.* Ti^{4+}, Nb^{5+}, and Ta^{5+}) *via* inductive effect [27–30]. Among various cations doped to perovskite oxynitrides, Mg^{2+} has been identified as one of the most effective dopants to improve the photocatalytic performance [11,31–34]. For instance, Mg doping can increase the O$_2$-evolution rate of LaTiO$_2$N and BaTaO$_2$N by a factor of 7 and 4, respectively [29,35]. In this work, Mg is introduced into BaNbO$_2$N to construct the solid solution series between BaNbO$_2$N and BaMg$_{1/3}$Nb$_{2/3}$O$_3$, *i.e.*, (BaNbO$_2$N)$_{1-x}$(BaMg$_{1/3}$Nb$_{2/3}$O$_3$)$_x$ ($0 \leq x \leq 1$), since Mg^{2+} has comparable cation size with Nb^{5+} and the parent compounds share similar crystal structures (space group: $Pm\bar{3}m$). The presence of Mg not only effectively suppresses the formation of defects such as Nb^{4+} which in turn, substantially ameliorates the photocarrier separation conditions in BaNbO$_2$N but also increases the surface

---

hydrophilicity. Moreover, the bandgap as well as band edge positions are also strongly correlated with Mg content which becomes a useful tool to manipulate the electronic structures of BaNbO$_2$N. As an exemplification for the practical application, Mg-modified BaNbO$_2$N has been merged into a Z-scheme system which is capable of stoichiometric overall water splitting under simulated AM 1.5 G illumination.

2. Experimental

2.1. Materials preparation

Solid solution series (BaNbO$_2$N)$_{1-x}$(BaMg$_{1/3}$Nb$_{2/3}$O$_3$)$_x$ ($0 \leq x \leq 1$) were prepared *via* a molten-salt assisted high-temperature ammonolysis approach. Reagent-grade KCl (SCR, 99.5 %) was selected as the salt for synthesis with a designated solute/solvent mass ratio of 1:2. Typically, for the preparation of (BaNbO$_2$N)$_{0.2}$(BaMg$_{1/3}$Nb$_{2/3}$O$_3$)$_{0.8}$ (x = 0.8), 0.2392 g BaCO$_3$ (Aladdin, 99 %), 0.0975 g Nb$_2$O$_5$ (Aladdin, 99.9 %), and 0.0230 g MgCO$_3$ (Urchem, 98 %) were ground thoroughly with 0.7194 g KCl. The Ba/(Mg+Nb) mole ratio was adjusted to be 1.2:1 in order to compensate barium volatilization and to suppress the possible generation of NbO$_x$N$_y$ during the high-temperature ammonolysis [36, 37]. The well-blended powders were then transferred into an alumina boat and were mounted into a tube furnace. The furnace was then ramped to 1223 K with a heating rate of 10 K min^{-1} under flowing ultrapure ammonia (flow rate: ~ 200 mL min^{-1}, Jiaya Chemicals, 99.999 %). After dwelling at 1223 K for 10 h, the furnace was cooled naturally to room temperature under flowing ultrapure ammonia. The resultant products were rinsed repeatedly with deionized water and ethanol to remove the residual salt. After dried at 353 K overnight, the powders were collected for further analysis. The parent compound BaMg$_{1/3}$Nb$_{2/3}$O$_3$ was also prepared under the similar conditions without high-temperature ammonolysis. The product was denoted as BMNO in order to be distinguished with the one that underwent high-temperature ammonolysis, *i.e.* BaMg$_{1/3}$Nb$_{2/3}$O$_{3-y}$N$_y$ (x = 1.0).

2.2. Materials characterizations

The phase purity and crystal structure of sample powders were analyzed on a Bruker D8 Focus diffractometer (Bruker, Germany) to collect their X-ray powder diffraction (XRD) patterns. Cu Kα$_1$ (λ = 1.5406 Å) and Cu Kα$_2$ (λ = 1.5444 Å) were used as the incident radiation. The crystal structure of sample powders was investigated by the Rietveld refinement of XRD data using the General Structure Analysis System (GSAS) software package [38]. A pseudo-Voigt function and the first type Chebyshev polynomial were adopted for profile and background fitting, respectively. Sample powders were further inspected under a field emission scanning electron microscope (FE-SEM, JSM-7900 F, Japan) and a transmission electron microscope (TEM, JEOL JEM-2100, Japan) for morphological and microstructural analyses. The particle size distribution of sample powders was determined based on a Nano Measure software. A NOVA 2200e adsorption instrument (Quantachrome, U.S.A.) was employed to measure and calculate the specific surface area of sample powders (pre-treated in vacuum at 473 K for 2 h) using the Brunauer–Emmett–Teller (BET) model. The contents of anions (oxygen and nitrogen) and cations (barium, magnesium, and niobium) in sample powders were respectively determined by an Elemental Analyzer (Unicube, Elementar, Germany) and an inductively coupled plasma optical emission spectrometry (ICP-OES, PE 8300). The ultraviolet-visible diffuse reflectance spectra (UV-Vis DRS) of sample powders were collected on an UV-Vis spectrophotometer (JASCO-750, Japan) equipped with an integrating sphere. BaSO$_4$ was used as the non-absorbing reference material. A Renishaw inVia Raman spectrometer and a Fourier transform infrared spectrometer (PittCon Thermo Scientific Nicolet iS20) were used to collect the Raman and Fourier-transform infrared spectra (FT-IR) of sample powders, respectively. The surface state of sample powders was analyzed by the X-ray

photoelectron spectroscopic (XPS) spectra (XPS, AXIS Ultra DLD, Japan, Al Kα source). XPS PEAKFIT software was used for XPS data fitting. Gaussian-Lorentzian (Lorentzian weighting of 20 %) functions were used for peak fit and background was assumed to be the Shirley-type. Adventitious carbon C 1 *s* peak at 284.7 eV was adopted for signal adjustment [39,40]. The wettability of sample powders was investigated on a Wetting Angle measuring instrument (Theta Flex, Biolin).

2.3. Photocatalytic activity tests

The photocatalytic activities of sample powders were examined in a top-irradiation-type reactor which is connected to a gas-closed circulation and evacuation system (Labsolar-6A, Perfect Light, P.R. China). The temperature of the reactor was kept at 281 K by a water jacket. A proper amount of CoO$_x$ was thermally deposited onto sample powders as a cocatalyst according to a previous report [15]. In a typical experiment, 0.1 g CoO$_x$-loaded sample powders were magnetically dispersed into 100 mL silver nitrate aqueous solution (0.05 M). The silver nitrate was used as an electron scavenger and the pH value was controlled at *c.a.* 8.5 by adding La$_2$O$_3$ (~ 0.2 g, Aladdin, 99.9 %). The reactor was evacuated for 40 min to remove air dissolved. Visible light photons (λ ≥ 420 nm) were used as the light source which was generated by filtering the output of a 300 W Xenon lamp (PLX-SXE300, Perfect Light, P.R. China) with a UV-cutoff filter. Likewise, the monochromatic light was used for the determination of apparent quantum efficiency (AQE). The monochromatic light was generated by filtering the output of a 300 W Xenon lamp with the bandpass filter at 420 nm, 450 nm, 500 nm, 550 nm, and 600 nm, respectively. The photon flux at individual monochromatic light was calibrated by a quantum meter (Apogee MP-300, USA). The AQE was then determined by the following equation (Eq. 1):

$$AQE = \frac{4R}{I} \times 100\% \tag{1}$$

where *R* and *I* represent the oxygen evolution rate at a specific wavelength (μmol·h^{-1}) and the photon flux (μmol·h^{-1}), respectively.

The experiment for the Z-scheme overall water splitting was carried out in the same setup. Typically, 50 mg Ru loaded SrTiO$_3$:Rh and 50 mg CoO$_x$ loaded (BaNbO$_2$N)$_{0.2}$(BaMg$_{1/3}$Nb$_{2/3}$O$_3$)$_{0.8}$ were dispersed into 100 mL FeCl$_3$ aqueous solution (2 mM). The pH value of the suspension system was adjusted to *c.a.* 2.5 by HCl. A 1 h pre-illumination was conducted before overall water splitting experiment which induces the partially conversion of Fe^{3+} to Fe^{2+} to form the Fe^{2+}/Fe^{3+} redox couple. In all experiments, the gas components within the reactor were determined by an on-line gas chromatograph (GC2014C, SHIMADZU, Japan) installed with a 5-Å molecular sieve columns, a TCD detector, and Ar as the carrier gas. The synthesis of SrTiO$_3$:Rh and the photo-deposition of 0.5 wt% Ru was referred to a previous work [41].

2.4. Photoelectrochemical (PEC) measurements

Sample powders were electrophoretically deposited onto a fluorine-doped tin oxide (FTO) glass to fabricate the semiconductor photoelectrodes according to a previous literature [42]. All PEC measurements were carried out on a CHI660E electrochemical workstation in a three-electrode configuration comprising the photoelectrode, Pt foil, and the Ag/AgCl electrode as the working, counter, and reference electrode, respectively. 0.1 mol L^{-1} KOH (25 mL, pH = 13) with or without sacrificial regent Na$_2$SO$_3$ (0.5 mol L^{-1}) was used as the electrolyte. A 300 W Xenon lamp (PLX-SXE300, Perfect Light, P. R. China) coupled with an UV (λ ≥ 420 nm) cut-off filter or AM 1.5 G filter was used as the light source. Electrochemical impedance spectra (EIS) at open circuit voltage were collected from 10^5 to 10^{-1} Hz with or without visible light illuminations. The open-circuit voltage decay (OCVD) profiles were recorded in Ar atmosphere and the photoelectrodes were firstly stored in the dark until a stable open-circuit voltage (V_{oc}) was

achieved. After illumination by visible light for 100 s, the photo-electrode was kept in the dark and the V_{oc} was allowed to decay back to its initial state. The flat band potential (E_{fb}) of the semiconductor photoelectrodes were determined from Mott-Schottky (MS) analysis. The MS plots were collected in the dark within a potential range of -0.2 V to 0.5 V (*vs.* reversible hydrogen electrode (RHE)) from 500 to 2000 Hz.

2.5. Theoretical calculations

The theoretical calculations of the band structures for BaNbO$_2$N, (BaNbO$_2$N)$_{0.2}$(BaMg$_{1/3}$Nb$_{2/3}$O$_3$)$_{0.8}$, and BMNO were achieved by density functional theory (DFT) using a commercial Vienna *ab initio* simulation package. The calculations were performed using the generalized gradient approximation (GGA), Perdew-Burke-Ernzerhof (PBE) function, and projector augmented-wave pseudopotential. A $2 \times 2 \times 2$ cubic unit cell ($a = b = c = 8.26$ Å, $\alpha = \beta = \gamma = 90°$) was used as the structure model. The structures were fully relaxed following the criteria that the forces on each atom are less than 0.02 eV·Å^{-1}. Mg/Nb and O/N were assumed to be completely disordered in the structure. An energy cutoff of 400 eV and a total energy of less than 10^{-5} eV were used for static electric potential calculations and geometry optimizations, respectively. A Monkhorst-Pack k-points mesh of $5 \times 5 \times 5$ was sampled for all structures.
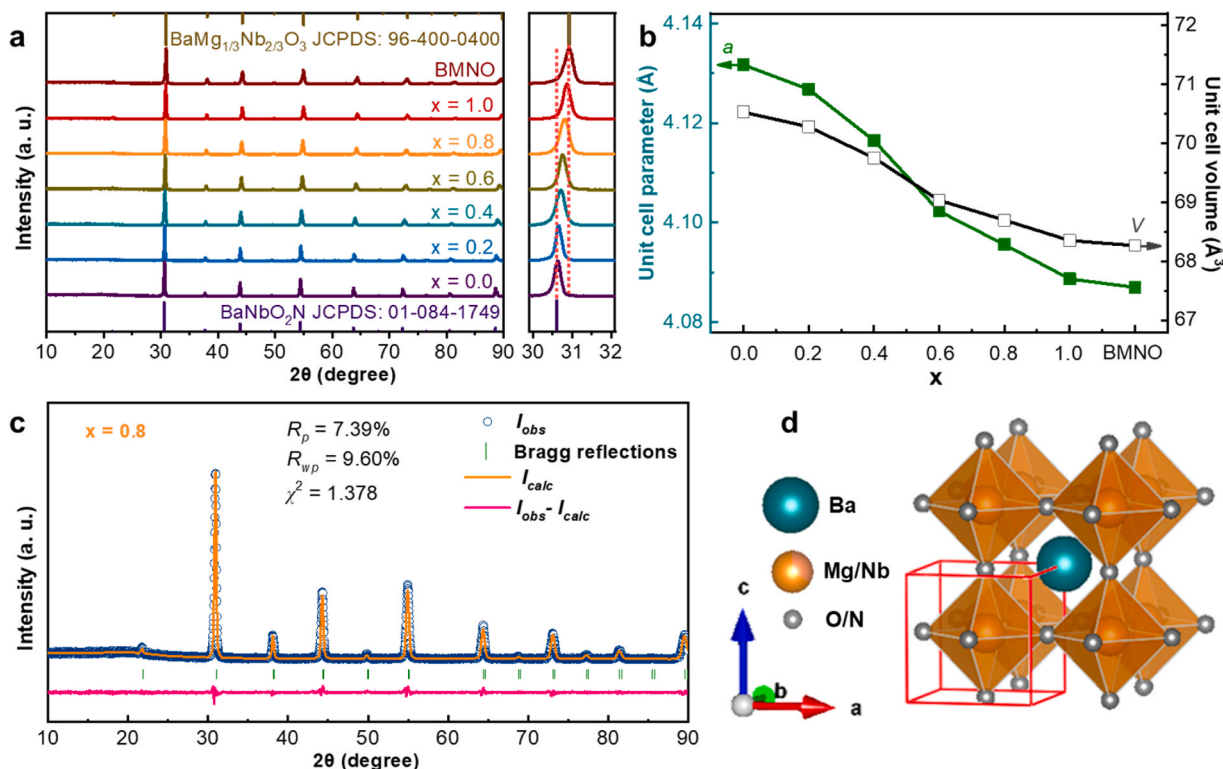
3. Results and discussion

3.1. Phase purity and crystal structures

The synthesis of BaNbO$_2$N is relatively more difficult than other perovskite oxynitrides as it lacks of a proper precursor that fulfils both a pentavalent charged Nb center and a stoichiometric Ba/Nb ratio [19,43, 44]. The relatively high electronegativity of Nb is susceptible to induce high defects concentration under high-temperature ammonia atmosphere [19,45]. Although using amorphous oxides as the precursor can ease the synthesis of BaNbO$_2$N because of their atomic dispersion, the product powders generally contain irregular-shaped agglomerates with abundant grain boundaries which are often harmful for inter-particle photocarrier transportations [22,46,47]. Here, BaNbO$_2$N and its solid solutions with BaMg$_{1/3}$Nb$_{2/3}$O$_3$ were synthesized by one-pot molten-salt assisted method under high-temperature ammonolysis. X-ray powder diffraction (XRD) analysis confirms that all samples are of pure phase and share the same XRD patterns with BaNbO$_2$N (JCPDS No. 01-064-1749) and BaMg$_{1/3}$Nb$_{2/3}$O$_3$ (JCPDS No. 96-400-0400) (Fig. 1a). Notably, there is a clear shift of all reflections toward high angles along with Mg incorporation, indicating shrinkage of unit cell for the solid solutions.

The crystal structures of sample powders were further studied by performing the Rietveld refinement on XRD data collected. Using the space group of $Pm\bar{3}m$, good agreement factors (R_p, R_{wp} and χ^2) were achieved under the constraints that Mg and Nb, O and N occupy the same crystallographic positions with the same isotropic temperature factors (inserted in Fig. 1c and Fig. S1). These results suggest that Mg dopants are randomly distributed at the B site as in the case of BaMg$_{1/3}$Nb$_{2/3}$O$_3$. Being consistent with previous deductions, the refined unit cell parameters decrease monotonically along with Mg uptake (Fig. 1b and Table S1). This phenomenon can be rationalized by the fact that doping one Mg^{2+} cation is accompanied by the substitution of three N^{3-} anions (ionic radius ~ 1.50 Å) with three O^{2-} anions (ionic radius ~1.40 Å) for charge balance, although Mg^{2+} (ionic radius ~ 0.72 Å) is slightly larger than Nb^{5+} (ionic radius ~ 0.64 Å). The typical refined XRD patterns for (BaNbO$_2$N)$_{0.2}$(BaMg$_{1/3}$Nb$_{2/3}$O$_3$)$_{0.8}$ ($x = 0.8$) were shown in Fig. 1c and Fig. 1d illustrates the corresponding refined crystal structure, suggesting a uniform occupation of Mg/Nb in the perovskite

Fig. 1. (a) XRD patterns of (BaNbO$_2$N)$_{1-x}$(BaMg$_{1/3}$Nb$_{2/3}$O$_3$)$_x$ ($0 \leq x \leq 1$) and BMNO. Standard XRD patterns of BaNbO$_2$N (JCPDS No. 01-064-1749) and BaMg$_{1/3}$Nb$_{2/3}$O$_3$ (JCPDS No. 96-400-0400) are also included for comparisons and the main reflection of (110) plane is enlarged on the right for clarity; (b) refined unit cell parameters of solid solution series (BaNbO$_2$N)$_{1-x}$(BaMg$_{1/3}$Nb$_{2/3}$O$_3$)$_x$ ($0 \leq x \leq 1$) and BMNO; (c) observed and calculated XRD patterns of (BaNbO$_2$N)$_{0.2}$(BaMg$_{1/3}$Nb$_{2/3}$O$_3$)$_{0.8}$ ($x = 0.8$), the agreement factors (R_p, R_{wp}, and χ^2) are shown as the insets; (d) typical refined crystal structure of (BaNbO$_2$N)$_{0.2}$(BaMg$_{1/3}$Nb$_{2/3}$O$_3$)$_{0.8}$ ($x = 0.8$) (the unit cell is marked by red lines).

lattice. The shrinkage of unit cells is beneficial for charge transportation because of the shortened M-O/N (M = Ti, Nb, and Ta *etc.*) bond lengths favoring orbital overlapping [26,48]. The random distribution of Mg/Nb cations and N/O anions, as well as the continuously strengthen of Nb-O/N bonds upon Mg modifications can be further verified by Fourier-transform infrared spectra (FT-IR) and Raman scattering analyses (Fig. S2).
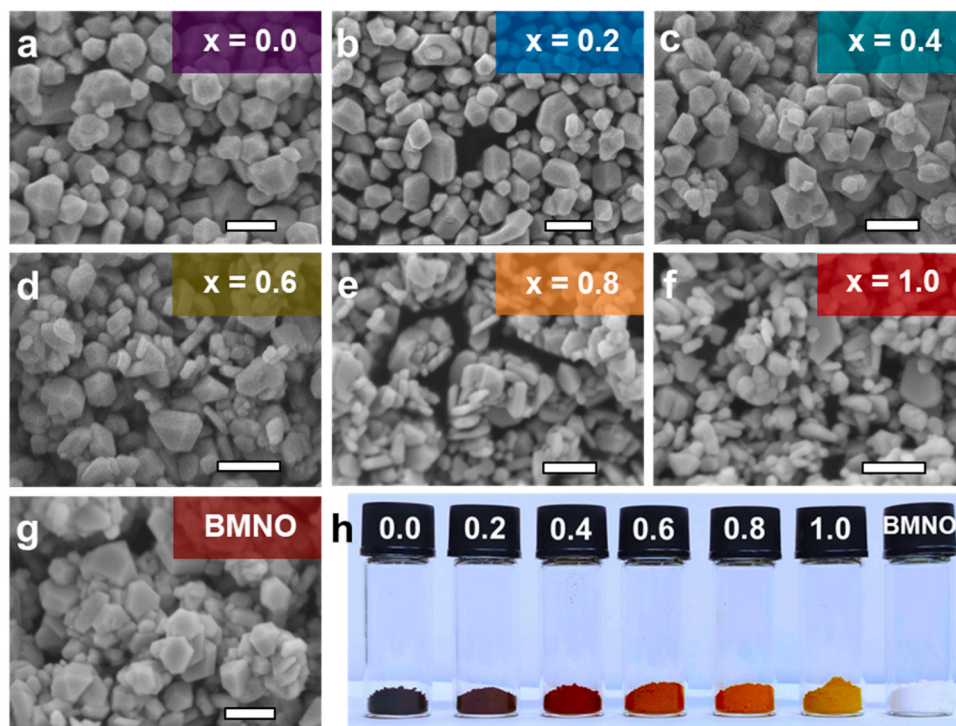
3.2. Microstructures

We continued to explore the morphology changes of sample particles after Mg incorporation. As can be seen from the field emission scanning electron microscopic (FE-SEM) images (Fig. 2a-g), all samples from $x = 0.0$ (BaNbO$_2$N) to 1.0 (BaMg$_{1/3}$Nb$_{2/3}$O$_{3-y}$N$_y$), including BMNO are composed of irregular-shaped particles with particle size of several hundred nanometers. Different crystal facets can be clearly identified for a single particle, thanks to the molten-salt environment that promotes the crystal growth. It's noteworthy that there is a clear correlation between particle size and Mg content (x), *i.e.*, particle size decreasing along with Mg content (Fig. S3a-h). This phenomenon is further evidenced by Brunauer-Emmett-Teller (BET) analysis (Fig. S4) where solid solutions have larger BET surface areas than BaNbO$_2$N. The difference between BMNO and $x = 1.0$ might be originated from N/O replacements which often introduce porous structure. Transmission electron microscopic (TEM) analysis further suggests the irregular-shaped particle morphology and the sample particles are of high crystallinity (Fig. S5). Moreover, the EDS elemental mapping analysis suggests the uniform distribution of Ba, Mg, Nb, O and N atoms within the sample particles (Fig. S6). The TEM-EDS analyses (Fig. S7), together with ICP-OES and ONH measurements (Table S2) verify all constituent elements are close to their stoichiometric values. These results consistently confirm the successful preparation of (BaNbO$_2$N)$_{1-x}$(BaMg$_{1/3}$Nb$_{2/3}$O$_3$)$_x$ ($0 \le x \le 1$) solid solutions *via* a one-pot flux-assisted high-temperature ammonolysis.

3.3. UV-Vis DRS spectra

Apart from particle morphologies, (BaNbO$_2$N)$_{1-x}$(BaMg$_{1/3}$Nb$_{2/3}$O$_3$)$_x$ ($0 \le x \le 1$) is also characterized by different sample colors (Fig. 2 h). The color of sample powders changes gradually from black, dark red, to yellow with increasing *x*, in contrast to the BMNO oxide which appears to be white. This phenomenon indicates that Mg content can effectively modulate the light absorption. This is further confirmed by their UV-Vis DRS spectra (Fig. 3a). BaNbO$_2$N exhibits a strong visible light absorption as far as 700 nm and an intense post-edge absorption tail beyond 700 nm. The post-edge absorption is considered to be the absorption of various types of defects (*e.g.* Nb^{4+} defects and *etc.*) and is in consistent with its black hue of sample powders [49,50]. It is evident that Mg incorporation effectively suppresses the intensity of the absorption tail, indicative of a decrement of defect concentration by Mg uptake. In addition, the absorption edges are gradually blue-shifted along with Mg incorporation, corresponding to the enlarged bandgaps. The bandgap of as-synthesized sample powders was then determined by the Tauc plot analysis (Fig. 3b) which shows a monotonic increment of bandgap values with Mg content. This can be rationalized by the decrement of N content by Mg incorporation as N 2*p* orbitals align at a higher energy position than O 2*p* orbitals, the hybridization of which contributes to the top of valence band.

3.4. Surface states and hydrophilicity

The surface state of sample powders is further investigated by X-ray photoelectron spectroscopic (XPS) analysis. The survey spectra of all sample powders of (BaNbO$_2$N)$_{1-x}$(BaMg$_{1/3}$Nb$_{2/3}$O$_3$)$_x$ ($0 \le x \le 1$) and BMNO confirm the presences of all constituent elements, particularly for Mg whose intensity increases with x as expected (Fig. S8a). The binding energies (BEs) of core-level electrons of Nb 3*d* can be deconvoluted into two distinct spin-orbit doublets assignable to the 3*d*$_{5/2}$ and 3*d*$_{3/2}$ states of Nb^{5+} and Nb^{4+} species (Fig. 4a). The doublet at lower BEs of 205.6 and 208.3 eV arises from Nb^{4+} species, and the other one at higher BEs of 206.8 and 209.5 eV belongs to Nb^{5+} species [18,22]. A high level of

Fig. 2. (a-g) FE-SEM images of (BaNbO2N)1-x(BaMg1/3Nb2/3O3)x ($0 \le x \le 1$) solid solutions, the scale bar is 500 nm; (h) digital photograph of sample powders of (BaNbO2N)1-x(BaMg1/3Nb2/3O3)x ($0 \le x \le 1$), the x value is labeled at the cap.
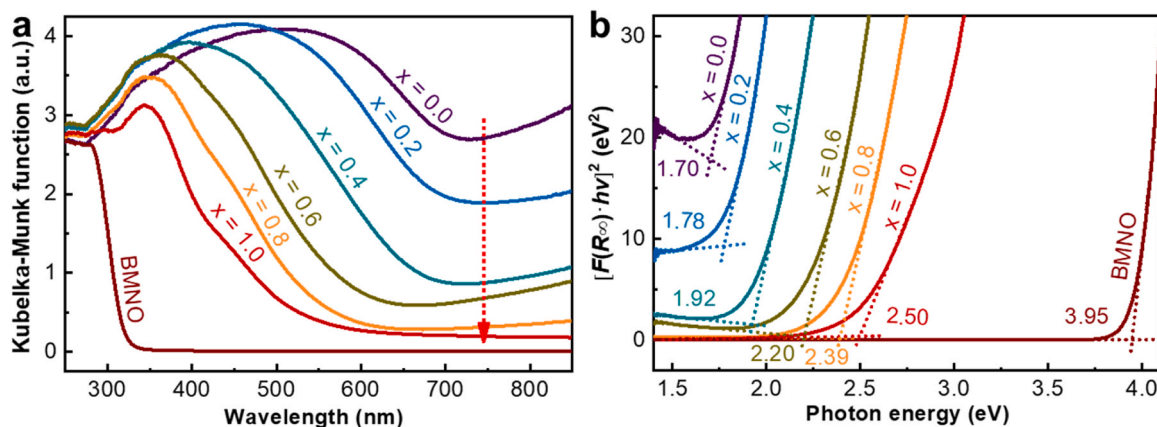
Fig. 3. (a) Ultraviolet-visible diffuse reflectance spectra (UV-Vis DRS) and (b) corresponding Tauc plot of $(BaNbO_2N)_{1-x}(BaMg_{1/3}Nb_{2/3}O_3)_x$ ($0 \leq x \leq 1$) solid solutions and BMNO.

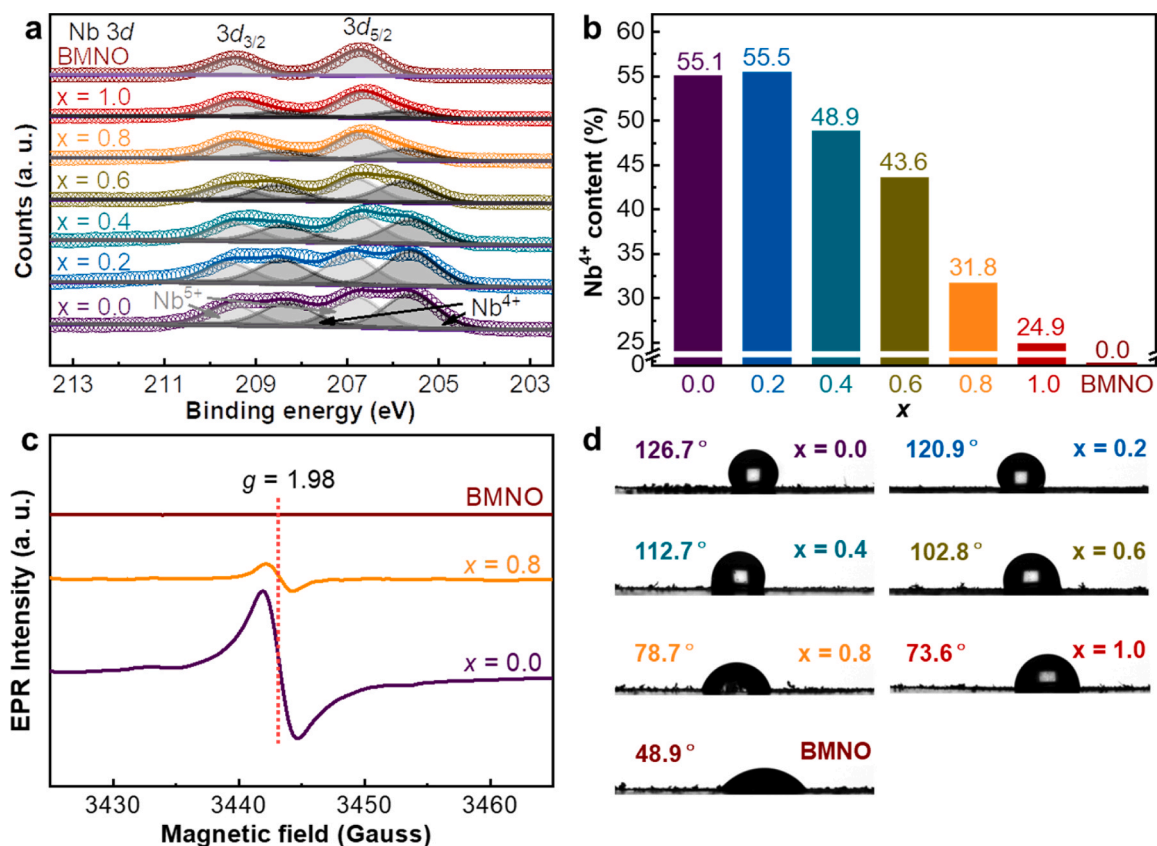**Fig. 4.** (a) X-ray photoelectron spectroscopic (XPS) spectra of $(BaNbO_2N)_{1-x}(BaMg_{1/3}Nb_{2/3}O_3)_x$ ($0 \leq x \leq 1$) solid solutions and BMNO in the Nb $3d$ region; (b) Nb^{4+} concentration as a function of $BaMg_{1/3}Nb_{2/3}O_3$ content; (c) electron paramagnetic resonance (EPR) analysis for $BaNbO_2N$ ($x = 0.0$), $(BaNbO_2N)_{0.2}(BaMg_{1/3}Nb_{2/3}O_3)_{0.8}$ ($x = 0.8$) and $BaMg_{1/3}Nb_{2/3}O_3$ (BMNO) at 100 K; (d) the wettability of $(BaNbO_2N)_{1-x}(BaMg_{1/3}Nb_{2/3}O_3)_x$ ($0 \leq x \leq 1$) solid solutions and BMNO.

Nb^{4+} species (55.1 %) are detected in pristine $BaNbO_2N$ ($x = 0.0$), and it decreases rapidly when solid solutions are formed (Fig. 4b). This is also confirmed by EPR analysis that the signal at a g factor of 1.98, assignable to paramagnetic Nb^{4+} species, decreases considerably after Mg incorporation (Fig. 4c). As pure $BaMg_{1/3}Nb_{2/3}O_3$ (BMNO) contains no Nb^{4+} defects, the Nb^{4+} defects arises from the high-temperature ammonolysis where Nb^{5+} cations are partially reduced [9,13]. The effective suppression of Nb^{4+} defects in solid solutions can be explained by the strong inductive effect of Mg, which increases the covalency of Nb–O(N) bonds and stabilizes Nb in a high valence. The shrinkage of unit cells, on the other hand, can be another reason as crystal stabilization energy of Nb

$(O,N)_6$ octahedrons is increased [51]. A detailed list of fitted parameters, including full width at half maxima (FWHMs) and BEs were tabulated in Table S3. Two overlapping peaks located at around 531.2 and 529.5 eV in the O 1 s spectra (Fig. S8b) are assigned to surface OH^- groups and lattice O^{2-} ions, respectively [52,53]. Although similar OH^-/O^{2-} ratios are suggested for all sample powders, the gradual increase of peak intensity upon Mg/O uptake indicates that there would be more OH^- groups at the surface of solid solutions, which suggests an improved surface hydrophilicity [48]. The wettability of a photocatalyst is of critical importance to its photocatalytic activity as hydroxyl groups often take part in water redox reactions. Accordingly, a photocatalyst
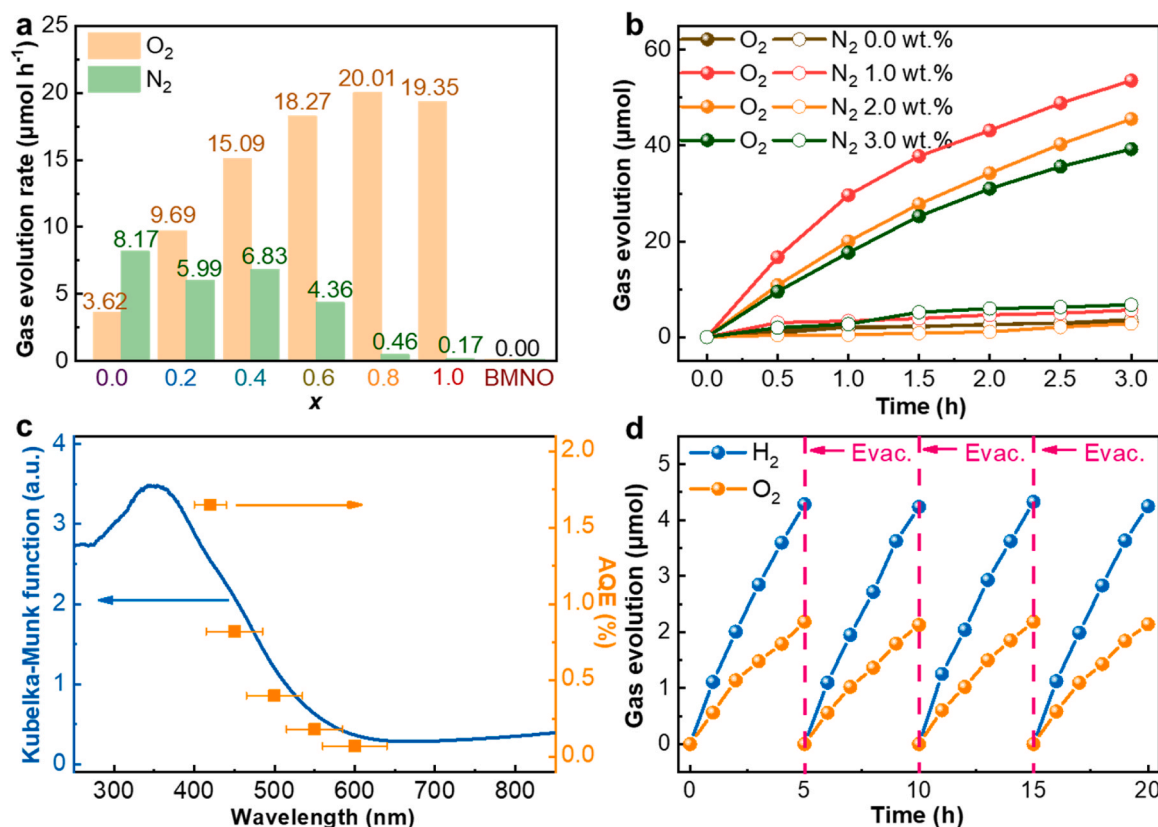
with a more hydrophilic surface is beneficial for water splitting [35]. The improvement of hydrophilicity/wettability was confirmed by water contact angle measurements (Fig. 4d). A smaller contact angle is observed for solid solutions than for pristine $BaNbO_2N$. The angles exceed 90° when $x \leq 0.6$, indicating that the surface is quite hydrophobic. By increasing Mg content, the samples turn to be hydrophilic when $x \geq 0.8$ [54]. The Mg $1s$ and N $1s$ states for $(BaNbO_2N)_{1-x}(BaMg_{1/3}Nb_{2/3}O_3)_x$ ($0 \leq x \leq 1$) both involve single broad peaks with either increased (Mg $1s$) or decreased (N $1s$) peak intensities, being consistent with the change of their contents (Fig. S8c and S8d). The continue loss of N can blue-shift the VBM as evidenced by the XPS valence band scan (Fig. S9).

3.5. Photocatalytic activities

Involving a four-electron transfer process, water oxidation reaction (OER) is sluggish in kinetics and is generally considered as the rate determining step for overall water splitting [55,56]. The photocatalytic activities of $(BaNbO_2N)_{1-x}(BaMg_{1/3}Nb_{2/3}O_3)_x$ ($0 \leq x \leq 1$) and BMNO were evaluated by probing their oxygen evolution from water using visible light photons ($\lambda \geq 420$ nm) as the energy source. 2 wt% CoO_x was loaded as a cocatalyst through impregnation and 0.05 M $AgNO_3$ aqueous solution was used to scavenge the photo-generated electrons. The suspension was adjusted to be slightly alkaline (pH ~ 8.5) by the hydrolysis of La_2O_3. No O_2 gases were detected in the absent of photocatalyst, light sources or water, thereby excluding any possible spontaneous O_2-releasing reactions. The photocatalytic O_2-evolution rate are plotted in Fig. 5 and Fig. S10. As shown in Fig. 5a, pristine $BaNbO_2N$ is poor in activity, producing small amounts of O_2 but more than doubled

amounts of N_2 during the first hour upon light illumination, being consistent with previous reports [17,22,44]. The incidental N_2-evolution is originated from the photo-oxidative self-decomposition of photocatalysts, which is probably due to the poor charger separation and/or transfer conditions of (oxy)nitrides [25,31,57]. Impressively, Mg incorporation not only boosts the photocatalytic activity, but also effectively alleviates the photo-corrosion phenomenon. For instance, $(BaNbO_2N)_{0.2}(BaMg_{1/3}Nb_{2/3}O_3)_{0.8}$ offers an oxygen evolution rate almost 6 times higher than that of $BaNbO_2N$ with a significantly inhibited N_2-evolution. The much-improved activity and stability of solid solutions are probably due to a combination of many beneficial properties of Mg incorporation, such as enlarged specific surface area, strengthened Nb-O/N bond, reduced Nb^{4+} defects, ameliorated hydrophilicity, and more positive VBM, *etc.* Nevertheless, the surface of $(BaNbO_2N)_{1-x}(BaMg_{1/3}Nb_{2/3}O_3)_x$ underwent partial oxidation after photocatalytic water oxidation reactions, although XRD and SEM analysis suggested no structure and microstructure changes (Figs. S11-S12). The XPS revealed that a fraction of Nb^{4+} species at the surface was oxidized into Nb^{5+} and the surface was probably reconstructed according to the change of Mg $1s$ and N $1s$ signals (Fig. S13). In addition, the side effect of introducing Mg is also evident as it enlarges the bandgap thereby reduces the usable photons from the light source. These considerations explain the optimal activity observed at x = 0.8 as there is a trade-off among various effects induced by Mg incorporation.

The photocatalytic activity of $(BaNbO_2N)_{0.2}(BaMg_{1/3}Nb_{2/3}O_3)_{0.8}$ can be further optimized by varying the amounts of CoO_x cocatalyst loaded (Fig. 5b). 1.0 wt% CoO_x was found to be the optimal loading content and was used for the further assessment of apparent quantum efficiency (AQE). The data for the calculation of AQE were tabulated in Table S4.

Fig. 5. Photocatalytic O_2- and N_2-evolution rate over $(BaNbO_2N)_{1-x}(BaMg_{1/3}Nb_{2/3}O_3)_x$ ($0 \leq x \leq 1$) solid solutions and BMNO after being loaded with 2 wt% CoO_x cocatalyst for the first hour of visible light illumination ($\lambda \geq 420$ nm) in 0.05 M $AgNO_3$ aqueous solution, 0.2 g La_2O_3 was added to maintain the pH at around 8.5; (b) temporal photocatalytic O_2 and N_2 production over $(BaNbO_2N)_{0.2}(BaMg_{1/3}Nb_{2/3}O_3)_{0.8}$ (x = 0.8) with varied CoO_x contents; (c) action spectra of $(BaNbO_2N)_{0.2}(BaMg_{1/3}Nb_{2/3}O_3)_{0.8}$ (x = 0.8) loaded with 1 wt% CoO_x for O_2 production; (d) overall water splitting under simulated solar insolation (AM 1.5 G) in a Z-scheme system constructed by using 1.0 wt% CoO_x loaded-$(BaNbO_2N)_{0.2}(BaMg_{1/3}Nb_{2/3}O_3)_{0.8}$ (x = 0.8) as the O_2-evolution moiety and 0.5 wt% Ru loaded-$SrTiO_3$:Rh as the H_2-evolution photocatalyst, Fe^{2+}/Fe^{3+} redox couple (0.002 M) was used as redox mediator and evacuation was performed every 5 h.

As shown in Fig. 5c, the dispersion of AQE agrees well with the UV-Vis DRS spectra, suggest a real photon-driven OER over $(BaNbO_2N)_{0.2}(BaMg_{1/3}Nb_{2/3}O_3)_{0.8}$. An AQE value as high as 1.65 % was achieved at 420 ± 20 nm, which outperforms most Nb-based perovskite oxynitrides reported to date (Table S5). Since $(BaNbO_2N)_{0.2}(BaMg_{1/3}Nb_{2/3}O_3)_{0.8}$ was efficient in photocatalyzing water into O_2, it was then employed as the O_2-evolution moiety to construct a Z-scheme system with a typical H_2-evolution photocatalyst, *i.e.*, SrTiO₃:Rh, using Fe^{2+}/Fe^{3+} redox couple as the mediator. Stable stoichiometric H_2/O_2 evolution from overall water splitting was achieved by the so-formed Z-scheme system under simulated solar insolation (AM 1.5 G) (Fig. 5d), holding great promise for solar energy conversion.
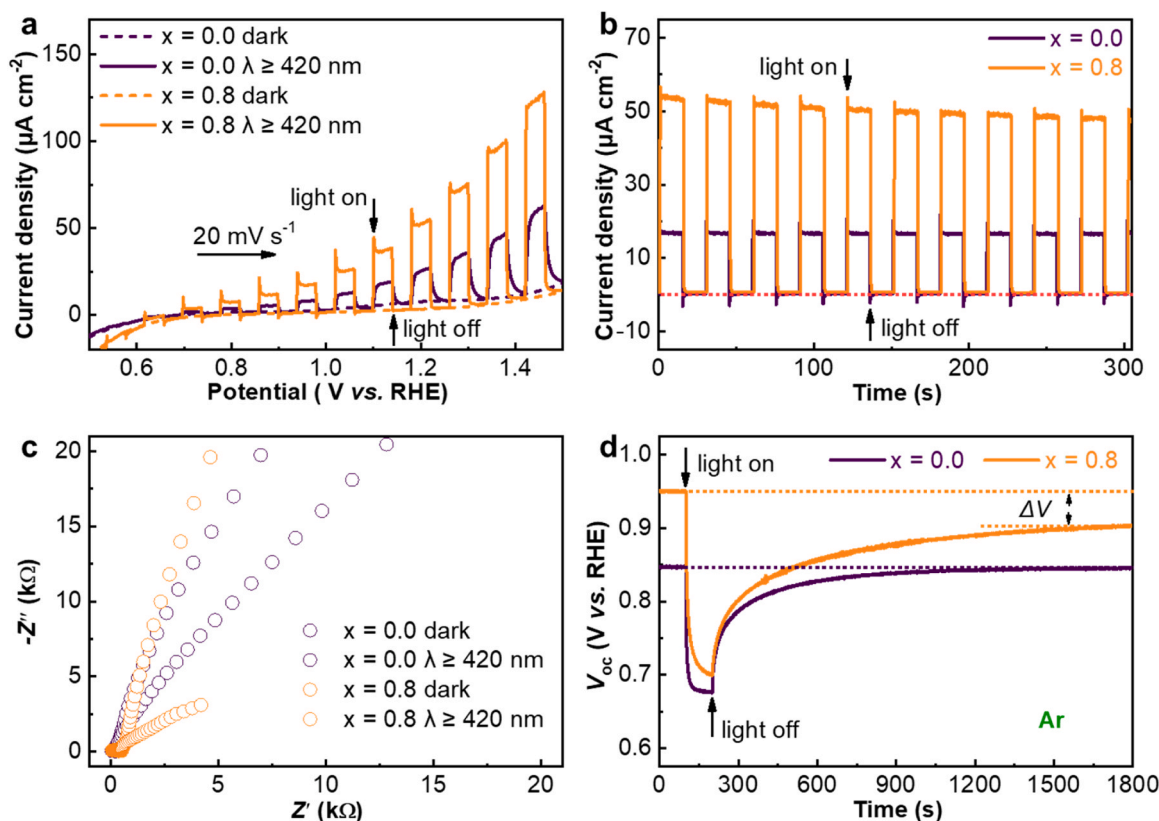
3.6. Photocarrier separation

For better understanding the improved photocatalytic activity of $BaNbO_2N$ after Mg incorporation, photoelectrochemical (PEC) measurements were performed to explore the photocarrier separation conditions of different samples. Firstly, linear sweep voltammetry (LSV) and chronoamperometry (i-t) under chopped visible light illuminations ($\lambda \geq 420$ nm) were applied to study the photocurrent. As shown in Fig. 6a-b, both pristine $BaNbO_2N$ and solid solution of $(BaNbO_2N)_{0.2}(BaMg_{1/3}Nb_{2/3}O_3)_{0.8}$ display a n-type semiconductivity with anodic photocurrents under positive bias. Apparently, $(BaNbO_2N)_{0.2}(BaMg_{1/3}Nb_{2/3}O_3)_{0.8}$ delivers a much higher photocurrent density than $BaNbO_2N$, which is in a good accordance with its improved photocatalytic activity. Moreover, the negative shift of onset potential for $(BaNbO_2N)_{0.2}(BaMg_{1/3}Nb_{2/3}O_3)_{0.8}$ implies that the photocarriers are easier to be separated, *i.e.*, improved charge separation conditions [33,58]. As $BaNbO_2N$ can strongly absorb visible light photons, its lower photocurrent indicates that there are severe charge recombination events in

the bulk or at the surface. Electrochemical impedance spectroscopy (EIS) under dark and/or visible light illumination ($\lambda \geq 420$ nm) was then conducted to investigate the charge transfer at the sample surface. The Nyquist plot for $(BaNbO_2N)_{0.2}(BaMg_{1/3}Nb_{2/3}O_3)_{0.8}$ exhibits a reduced interfacial charge transfer resistance compared to $BaNbO_2N$ under light illumination (Fig. 6c), indicating a better charge transfer process at its surface. This is probably originated from its larger specific surface area or improved surface hydrophilicity [59]. Open-circuit voltage (V_{oc}) decay (OCVD) experiments performed in Ar atmosphere offer more useful information on charge separation [23,30]. As observed in the OCVD profile (Fig. 6d), $BaNbO_2N$ and $(BaNbO_2N)_{0.2}(BaMg_{1/3}Nb_{2/3}O_3)_{0.8}$ manifest a negative shift of V_{oc} upon light illumination, confirming again their n-type semiconductivity. In sharp contrast to $BaNbO_2N$ which quickly restores the V_{oc} back to the dark value upon light off, $(BaNbO_2N)_{0.2}(BaMg_{1/3}Nb_{2/3}O_3)_{0.8}$ demonstrates a much slower V_{oc} restoration process even longer than 1600 s. This observation further reveals the severe charge recombination evens in pristine $BaNbO_2N$ which can be considerably suppressed by Mg incorporation [30].

The efficiencies for both charge separation and transfer processes were further quantified by probing the LSV curves with the assistant of Na_2SO_3 (Fig. 7a-b) [8,60,61]. The overall efficiency (η) is determined by the multiplication of the efficiencies in light absorption ($\eta_{absorption}$), bulk charge separation (η_{bulk}) and interfacial charge transfer ($\eta_{surface}$) processes as following equation (Eq. 2) [1,62]:
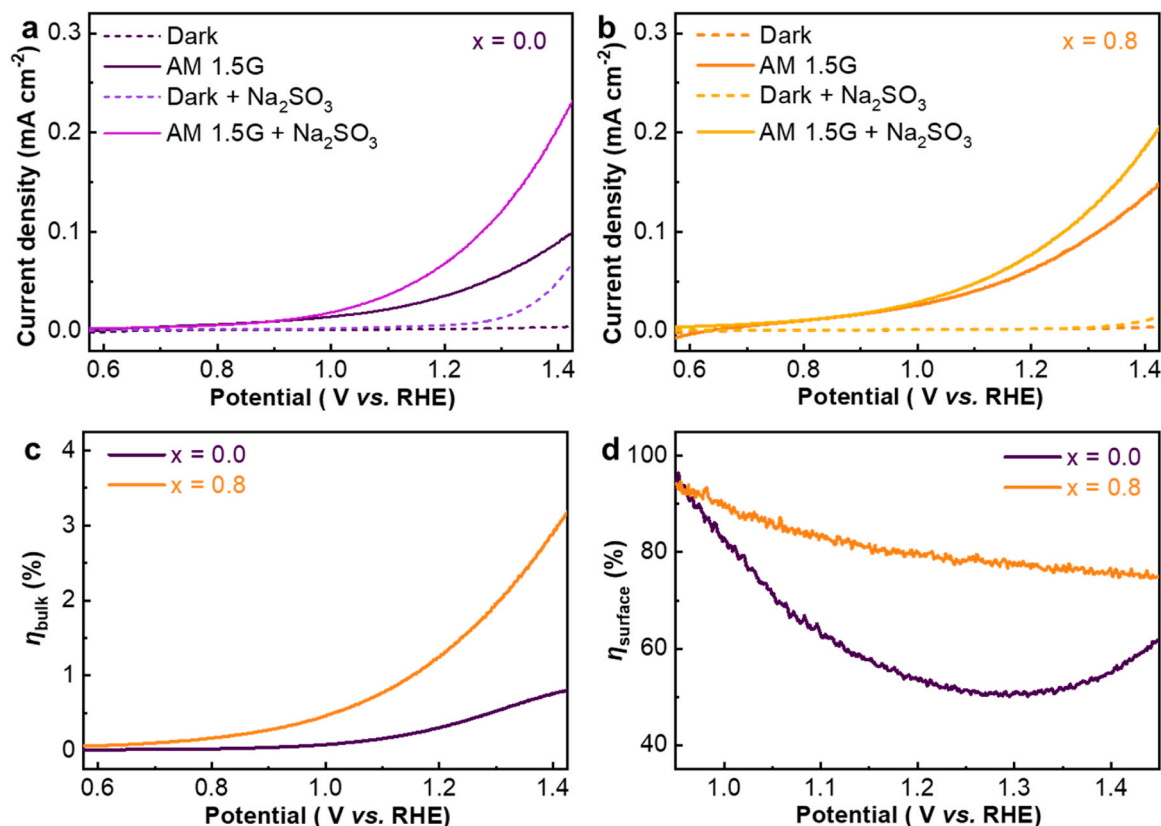
$$J = J_{abs} \bullet \eta_{bulk} \times \eta_{surface} \tag{2}$$

In which J and J_{abs} respectively represent the determined photocurrent density and theoretical photocurrent density of photoelectrode materials [59]. The symbol " $\times$ " between η_{bulk} and $\eta_{surface}$ implies there

Fig. 6. Linear sweep voltammetry (LSV) curves of photoelectrodes electrophoretically deposited from sample powders of $BaNbO_2N$ (x = 0.0) and $(BaNbO_2N)_{0.2}(BaMg_{1/3}Nb_{2/3}O_3)_{0.8}$ (x = 0.8); (b) amperometric i-t curves of $BaNbO_2N$ (x = 0.0) and $(BaNbO_2N)_{0.2}(BaMg_{1/3}Nb_{2/3}O_3)_{0.8}$ (x = 0.8) at 1.23 V *vs.* RHE; (c) electrochemical impedance spectra (EIS) of $BaNbO_2N$ (x = 0.0) and $(BaNbO_2N)_{0.2}(BaMg_{1/3}Nb_{2/3}O_3)_{0.8}$ (x = 0.8) at open-circuit voltage in the dark and under visible light illumination ($\lambda \geq 420$ nm); (d) open-circuit voltage decay (OCVD) profile of $BaNbO_2N$ (x = 0.0) and $(BaNbO_2N)_{0.2}(BaMg_{1/3}Nb_{2/3}O_3)_{0.8}$ (x = 0.8) in Ar atmosphere.

Fig. 7. LSV curves of (a) BaNbO$_2$N (x = 0.0) and (b) (BaNbO$_2$N)$_{0.2}$(BaMg$_{1/3}$Nb$_{2/3}$O$_3$)$_{0.8}$ (x = 0.8) in the dark or under simulated AM 1.5 G illuminations with or without Na$_2$SO$_3$; (c) charge separation efficiency (η_{bulk}) and (d) interfacial charge transfer efficiency ($\eta_{surface}$) of BaNbO$_2$N (x = 0.0) and (BaNbO$_2$N)$_{0.2}$(BaMg$_{1/3}$Nb$_{2/3}$O$_3$)$_{0.8}$ (x = 0.8).

exists a synergetic effect between them. The J_{abs} values for BaNbO$_2$N ($J_{0.0}$) and (BaNbO$_2$N)$_{0.2}$(BaMg$_{1/3}$Nb$_{2/3}$O$_3$)$_{0.8}$ ($J_{0.8}$) are calculated to be 20.45 and 6.00 mA cm^{-2} (Fig. S14). The photocurrent density measured in the presence of Na$_2$SO$_3$ is assumed a net contribution of bulk charge separation because of the fast oxidation kinetics of Na$_2$SO$_3$. Therefore, η_{bulk} can be acquired through a division operation between measured photocurrent density ($J_{KOH+Na_2SO_3}$) and J_{abs}. Subsequently, the $\eta_{surface}$ can be also calculated by dividing J_{KOH} with $J_{KOH+Na_2SO_3}$ [60]. The η_{bulk} for (BaNbO$_2$N)$_{0.2}$(BaMg$_{1/3}$Nb$_{2/3}$O$_3$)$_{0.8}$ is almost fourfold higher than that for pristine BaNbO$_2$N at 1.23 V *vs.* RHE, verifying again the improved photocarrier separation (Fig. 7c). In addition, the $\eta_{surface}$ has also been improved (Fig. 7d), which can be attributed to a larger specific surface area and meliorated surface hydrophilicity. Thereby, the improved photocatalytic activity of (BaNbO$_2$N)$_{0.2}$(BaMg$_{1/3}$Nb$_{2/3}$O$_3$)$_{0.8}$ is a joint contribution of the increased η_{bulk} and $\eta_{surface}$.

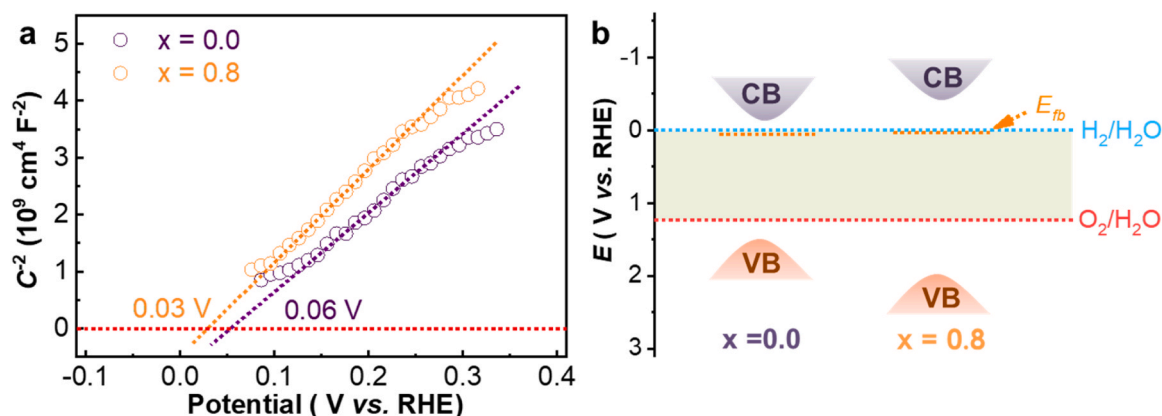*3.7. Band structures and band edge positions*

The impact of Mg modification on the electronic structure of BaNbO$_2$N was investigated by density functional theory (DFT) calculations. As presented in Fig. 8, the calculated band structures of all samples confirm their semiconductivity with bandgaps of 0.45 eV, 1.96 eV, and 2.20 eV for BaNbO$_2$N, (BaNbO$_2$N)$_{0.2}$(BaMg$_{1/3}$Nb$_{2/3}$O$_3$)$_{0.8}$, and BMNO, respectively. The deviation of calculated bandgaps with respect to the experimental ones is known for GGA method which often underestimates the bandgaps [63,64]. Nevertheless, the trend of bandgap enlargement after introducing Mg is consistent with the experimental observations. DOS analysis suggests that the band structures of all three samples close to Fermi levels are mainly composed by Nb 3d orbitals for conduction band (CB) and hybridized O 2p/N 2p orbitals for valence band (VB). Although Mg does not contribute directly to the formation of

VB and CB, it modifies the position of VB by modulating O/N ratio and narrowing the bandwidth of CB that mainly formed by Nb 4d orbitals, which is in good accordance with previous observations [29,35].

The band edge positions of samples were further determined through the combination of Mott-Schottky (MS) and XPS valence band scan analysis. Fig. 9a illustrates the MS curves of BaNbO$_2$N and (BaNbO$_2$N)$_{0.2}$(BaMg$_{1/3}$Nb$_{2/3}$O$_3$)$_{0.8}$, in which both samples have positive slops, confirming again their n-type semiconductivity. The slop for (BaNbO$_2$N)$_{0.2}$(BaMg$_{1/3}$Nb$_{2/3}$O$_3$)$_{0.8}$ is slightly larger than that for BaNbO$_2$N, indicating an decreased donor concentration in the former [26]. By extrapolating the MS curves down to energy axis, the flat band potentials (E_{fb}) of BaNbO$_2$N and (BaNbO$_2$N)$_{0.2}$(BaMg$_{1/3}$Nb$_{2/3}$O$_3$)$_{0.8}$ were determined to be 0.06 and 0.03 V *vs* RHE, respectively. Recalling the XPS valance band scan analysis which suggests the energy gap between VBM and Fermi level, the band edge positions for pristine BaNbO$_2$N and (BaNbO$_2$N)$_{0.2}$(BaMg$_{1/3}$Nb$_{2/3}$O$_3$)$_{0.8}$ can be determined. A schematic illustration of band edge positions is presented in Fig. 9b. It can be seen from Fig. 9b that both samples have proper CBM and VBM positions that are thermodynamically feasible for water redox reactions. Compared with pristine BaNbO$_2$N, a more positive alignment of VBM for (BaNbO$_2$N)$_{0.2}$(BaMg$_{1/3}$Nb$_{2/3}$O$_3$)$_{0.8}$ is noticed which suggests a higher energetics of photo-generated holes for OER, being likely another impetus to its activity enhancement. Being consistent with DFT calculations, the CBM of (BaNbO$_2$N)$_{0.2}$(BaMg$_{1/3}$Nb$_{2/3}$O$_3$)$_{0.8}$ has been negatively shifted due to the continuous replacement of Nb^{5+} with Mg^{2+}, indicating a stronger reductive force of photo-generated electrons. Although the CBMs for both samples are properly aligned for HER, the attempts to produce hydrogen from water failed even Pt cocatalyst was loaded. This is probably due to the severe trapping of photo-generated electrons by defects that prevent effective charge transfer to surface Pt cocatalyst [65].

Fig. 8. Band structures, density of states (DOS) and projected density of states (PDOS) for (a) BaNbO$_2$N (x = 0.0); (b) (BaNbO$_2$N)$_{0.2}$(BaMg$_{1/3}$Nb$_{2/3}$O$_3$)$_{0.8}$ (x = 0.8); (c) BaMgNbO$_3$ (BMNO), Fermi level is marked by the dotted lines.

Fig. 9. (a) Mott-Schottky (MS) plots of $BaNbO_2N$ (x = 0.0) and $(BaNbO_2N)_{0.2}(BaMg_{1/3}Nb_{2/3}O_3)_{0.8}$ (x = 0.8) at a fixed frequency of 1000 Hz, flat band potential (E_{fb}) is determined by extrapolating the MS curves down to energy axis; (b) schematic illustration of band edge positions of $BaNbO_2N$ (x = 0.0) and $(BaNbO_2N)_{0.2}(BaMg_{1/3}Nb_{2/3}O_3)_{0.8}$ (x = 0.8), water redox potentials are also included.

4. Conclusions

Solid solutions between $BaNbO_2N$ and $BaMg_{1/3}Nb_{2/3}O_3$, *i.e.*, $(BaNbO_2N)_{1-x}(BaMg_{1/3}Nb_{2/3}O_3)_x$ ($0 \leq x \leq 1$) have been successfully synthesized *via* a one-pot molten-salt assisted high-temperature ammonolysis. Compared with parent compound $BaNbO_2N$, introducing Mg to the perovskite lattice leads to enlarged bandgaps, reduced defect concentration, increased specific surface areas and improved hydrophilicity, which in turn contribute to an improved photocatalytic activity for OER with high stability. An AQE value as high as 1.65 % at 420 ± 20 nm was recorded over $(BaNbO_2N)_{0.2}(BaMg_{1/3}Nb_{2/3}O_3)_{0.8}$ (x = 0.8) under optimal conditions, outperforming most Nb-based perovskite oxynitride photocatalysts reported to date. Moreover, a Z-scheme system comprising $(BaNbO_2N)_{0.2}(BaMg_{1/3}Nb_{2/3}O_3)_{0.8}$ (*x* = 0.8) as the O_2-evolution moiety can steadily photocatalyze overall water splitting into stoichiometric H_2 and O_2 under simulated solar insolation.

CRediT authorship contribution statement

Lin Yang performed the experiments, analyzed the data, and wrote the manuscript. **Zhuo Li** did the DFT calculation. **Xiaoxiang Xu** guided project and revised the manuscript.

Declaration of Competing Interest

The authors declare that they have no known competing financial interests or personal relationships that could have appeared to influence the work reported in this paper.

Data availability

Data will be made available on request.

Acknowledgements

Appendix A. Supporting information

Supplementary data associated with this article can be found in the online version at doi:10.1016/j.apcatb.2023.123221.

References

[1] X.P. Tao, Y. Zhao, S.Y. Wang, C. Li, R.G. Li, Recent advances and perspectives for solar-driven water splitting using particulate photocatalysts, Chem. Soc. Rev. 51 (2022) 3561–3608, https://doi.org/10.1039/D1CS01182K.

[2] B.B. Dong, J.Y. Cui, Y. Qi, F.X. Zhang, Nanostructure engineering and modulation of (oxy)nitrides for application in visible-light-driven water splitting, Adv. Mater. 33 (2021), 2004697, https://doi.org/10.1002/adma.202004697.

[3] K.H. Chen, J.D. Xiao, J.J.M. Vequizo, T. Hisatomi, Y.W. Ma, M. Nakabayashi, T. Takata, A. Yamakata, N. Shibata, K. Domen, Overall water splitting by a SrTaO₂N-based photocatalyst decorated with an Ir-promoted Ru-based cocatalyst, J. Am. Chem. Soc. 145 (2023) 3839–3843, https://doi.org/10.1021/jacs.2c11025.

[4] Y.W. Wang, Y.Y. Kang, H.Z. Zhu, G. Liu, J.T.S. Irvine, X.X. Xu, Perovskite oxynitride solid solutions of LaTaON₂-CaTaO₂N with greatly enhanced photogenerated charge separation for solar-driven overall water splitting, Adv. Sci. 8 (2021), 2003343, https://doi.org/10.1002/advs.202003343.

[5] Y.F. Bao, S.W. Du, Y. Qi, G. Li, P. Zhang, G.S. Shao, F.X. Zhang, Synthesis of a visible-light-responsive perovskite SmTiO₂N bifunctional photocatalyst via an evaporation-assisted layered-precursor strategy, Adv. Mater. 33 (2021), 2101883, https://doi.org/10.1002/adma.202101883.

[6] Y.F. Bao, C. Li, K. Domen, F.X. Zhang, Strategies and methods of modulating nitrogen-incorporated oxide photocatalysts for promoted water splitting, Acc. Mater. Res. 3 (2022) 449–460, https://doi.org/10.1021/accountsmr.1c00271.

[7] S.S. Chen, T. Takata, K. Domen, Particulate photocatalysts for overall water splitting, Nat. Rev. Mater. 2 (2017) 17050, https://doi.org/10.1038/Natrevmats.2017.50.

[8] S.F. Chang, J.X. Yu, R. Wang, Q.Y. Fu, X.X. Xu, LaTaON₂ mesoporous single crystals for efficient photocatalytic water oxidation and Z-scheme overall water splitting, ACS Nano 15 (2021) 18153–18162, https://doi.org/10.1021/acsnano.1c06871.

[9] L. Yang, J.X. Yu, Q.Y. Fu, L.L. Kong, X.X. Xu, Mesoporous single-crystalline SrNbO₂N: expediting charge transportation to advance solar water splitting, Nano Energy 95 (2022), 107059, https://doi.org/10.1016/j.nanoen.2022.107059.

[10] K. Maeda, D.L. Lu, K. Domen, Oxidation of water under visible-light irradiation over modified BaTaO₂N photocatalysts promoted by tungsten species, Angew. Chem. Int. Ed. 52 (2013) 6488–6491, https://doi.org/10.1002/anie.201301357.

[11] H.H. Li, J.D. Xiao, J.J.M. Vequizo, T. Hisatomi, M. Nakabayashi, Z.H. Pan, N. Shibata, A. Yamakata, T. Takata, K. Domen, One-step excitation overall water splitting over a modified Mg-doped BaTaO₂N photocatalyst, ACS Catal. 12 (2022) 10179–10185, https://doi.org/10.1021/acscatal.2c02394.

[12] X. Wang, T. Hisatomi, J.W. Liang, Z. Wang, Y.J. Xiang, Y.H. Zhao, X.Y. Dai, T. Takata, K. Domen, Facet engineering of LaNbON2 transformed from LaKNaNbO5 for enhanced photocatalytic O2 evolution, J. Mater. Chem. A 8 (2020) 11743–11751, https://doi.org/10.1039/D0TA01489C.

[13] J.X. Yu, X.X. Xu, LaNbON₂ mesoporous single crystals with expedited photocarrier separation for efficient visible-light-driven water redox reactions, J. Catal. 413 (2022) 858–869, https://doi.org/10.1016/j.jcat.2022.07.033.

[14] M. Higashi, K. Domen, R. Abe, Fabrication of an efficient BaTaO₂N photoanode harvesting a wide range of visible light for water splitting, J. Am. Chem. Soc. 135 (2013) 10238–10241, https://doi.org/10.1021/ja404030x.

[15] F.X. Zhang, A. Yamakata, K. Maeda, Y. Moriya, T. Takata, J. Kubota, K. Teshima, S. Oishi, K. Domen, Cobalt-modified porous single-crystalline LaTiO₂N for highly efficient water oxidation under visible light, J. Am. Chem. Soc. 134 (2012) 8348–8351, https://doi.org/10.1021/ja301726c.

[16] M. Matsukawa, R. Ishikawa, T. Hisatomi, Y. Moriya, N. Shibata, J. Kubota, Y. Ikuhara, K. Domen, Enhancing photocatalytic activity of LaTiO₂N by removal of surface reconstruction layer, Nano. Lett. 14 (2014) 1038–1041, https://doi.org/10.1021/nl404688h.

[17] M. Hojamberdiev, E. Zahedi, E. Nurlaela, K. Kawashima, K. Yubuta, M. Nakayama, H. Wagata, T. Minegishi, K. Domen, K. Teshima, The cross-substitution effect of tantalum on the visible-light-driven water oxidation activity of BaNbO₂N crystals

grown directly by an NH$_3$-assisted flux method, J. Mater. Chem. A 4 (2016) 12807–12817, https://doi.org/10.1039/C6TA03786K.

[18] K. Kawashima, M. Hojamberdiev, K. Yubuta, K. Domen, K. Teshima, Synthesis and visible-light-induced sacrificial photocatalytic water oxidation of quinary oxynitride BaNb$_{0.5}$Ta$_{0.5}$O$_2$N crystals, J. Energy Chem. 27 (2018) 1415–1421, https://doi.org/10.1016/j.jechem.2017.09.006.

[19] J. Seo, Y. Moriya, M. Kodera, T. Hisatomi, T. Minegishi, M. Katayama, K. Domen, Photoelectrochemical water splitting on particulate ANbO$_2$N (A = Ba, Sr) photoanodes prepared from perovskite-type ANbO$_3$, Chem. Mater. 28 (2016) 6869–6876, https://doi.org/10.1021/acs.chemmater.6b02091.

[20] B. Siritanaratkul, K. Maeda, T. Hisatomi, K. Domen, Synthesis and photocatalytic activity of perovskite niobium oxynitrides with wide visible-light absorption bands, ChemSusChem 4 (2011) 74–78, https://doi.org/10.1002/cssc.201000207.

[21] J. Seo, D. Ishizuka, T. Hisatomi, T. Takata, K. Domen, Effect of Mg^{2+} substitution on the photocatalytic water splitting activity of LaMg$_x$Nb$_{1-x}$O$_{1+3x}$N$_{2-3x}$, J. Mater. Chem. A 9 (2021) 8655–8662, https://doi.org/10.1039/D1TA00164G.

[22] S.H. Wei, S. Jin, G.X. Pan, Z.X. Li, G. Liu, X.X. Xu, Triggering efficient photocatalytic water oxidation reactions over BaNbO$_2$N by incorporating Ca at B site, J. Am. Ceram. Soc. 102 (2019) 6194–6201, https://doi.org/10.1111/jace.16485.

[23] S.H. Wei, G. Zhang, X.X. Xu, Activating BaTaO$_2$N by Ca modifications and cobalt oxide for visible light photocatalytic water oxidation reactions, Appl. Catal. B Environ. 237 (2018) 373–381, https://doi.org/10.1016/j.apcatb.2018.06.017.

[24] Y.W. Wang, S.H. Wei, X.X. Xu, SrTaO$_2$N-CaTaO$_2$N solid solutions as efficient visible light active photocatalysts for water oxidation and reduction, Appl. Catal. B Environ. 263 (2020), 118315, https://doi.org/10.1016/j.apcatb.2019.118315.

[25] C. Pan, T. Takata, K. Kumamoto, S.S.K. Ma, K. Ueda, T. Minegishi, M. Nakabayashi, T. Matsumoto, N. Shibata, Y. Ikuhara, K. Domen, Band engineering of perovskite-type transition metal oxynitrides for photocatalytic overall water splitting, J. Mater. Chem. A 4 (2016) 4544–4552, https://doi.org/10.1039/C5TA10612E.

[26] X.Q. Sun, G. Liu, X.X. Xu, Defect management and efficient photocatalytic water oxidation reaction over Mg modified SrNbO$_2$N, J. Mater. Chem. A 6 (2018) 10947–10957, https://doi.org/10.1039/C8TA00767E.

[27] F.F. Wu, G. Liu, X.X. Xu, Efficient photocatalytic oxygen production over Ca-modified LaTiO$_2$N, J. Catal. 346 (2017) 10–20, https://doi.org/10.1016/j.jcat.2016.11.022.

[28] F.F. Wu, X.Q. Sun, G. Liu, X.X. Xu, Actualizing efficient photocatalytic water oxidation over SrTaO$_2$N by Na modification, Catal. Sci. Technol. 7 (2017) 4640–4647, https://doi.org/10.1039/C7CY01580A.

[29] H. Zhang, S.H. Wei, X.X. Xu, Mg modified BaTaO$_2$N as an efficient visible-light-active photocatalyst for water oxidation, J. Catal. 383 (2020) 135–143, https://doi.org/10.1016/j.jcat.2020.01.005.

[30] Y.W. Wang, S. Jin, X.Q. Sun, S.H. Wei, L. Chen, X.X. Xu, Switching on efficient photocatalytic water oxidation reactions over CaNbO$_2$N by Mg modifications under visible light illumination, Appl. Catal. B Environ. 245 (2019) 10–19, https://doi.org/10.1016/j.apcatb.2018.12.033.

[31] C.S. Pan, T. Takata, M. Nakabayashi, T. Matsumoto, N. Shibata, Y. Ikuhara, K. Domen, A complex perovskite-type oxynitride: the first photocatalyst for water splitting operable at up to 600 nm, Angew. Chem. Int. Ed. 54 (2015) 2955–2959, https://doi.org/10.1002/anie.201410961.

[32] Y.H. Xie, Y.W. Wang, Z.F. Chen, X.X. Xu, Role of oxygen defects on the photocatalytic properties of Mg-doped mesoporous Ta$_3$N$_5$, ChemSusChem 9 (2016) 1403–1412, https://doi.org/10.1002/cssc.201600193.

[33] Y.Q. Xiao, C. Feng, J. Fu, F.Z. Wang, C.L. Li, V.F. Kunzelmann, C.M. Jiang, M. Nakabayashi, N. Shibata, I.D. Sharp, K. Domen, Y.B. Li, Band structure engineering and defect control of Ta$_3$N$_5$ for efficient photoelectrochemical water oxidation, Nat. Catal. 3 (2020) 932–940, https://doi.org/10.1038/s41929-020-00522-9.

[34] Y.Q. Xiao, Z.Y. Fan, M. Nakabayashi, Q.Q. Li, L.J. Zhou, Q. Wang, C.L. Li, N. Shibata, K. Domen, Y.B. Li, Decoupling light absorption and carrier transport via heterogeneous doping in Ta$_3$N$_5$ thin film photoanode, Nat. Commun. 13 (2022) 7769, https://doi.org/10.1038/s41467-022-35538-1.

[35] G.A. Lin, X.Q. Sun, X.X. Xu, Mg modified LaTiO$_2$N with ameliorated photocarrier separation for solar water splitting, Appl. Catal. B Environ. 324 (2023) 122258, https://doi.org/10.1016/j.apcatb.2022.122258.

[36] T. Hisatomi, C. Katayama, K. Teramura, T. Takata, Y. Moriya, T. Minegishi, M. Katayama, H. Nishiyama, T. Yamada, K. Domen, The effects of preparation conditions for a BaNbO$_2$N photocatalyst on its physical properties, ChemSusChem 7 (2014) 2016–2021, https://doi.org/10.1002/cssc.201400121.

[37] Y. Luo, S. Suzuki, Z. Wang, K. Yubuta, J.J.M. Vequizo, A. Yamakata, H. Shiiba, T. Hisatomi, K. Domen, K. Teshima, Construction of spatial charge separation facets on BaTaO$_2$N crystals by flux growth approach for visible-light-driven H$_2$ production, ACS Appl. Mater. Inter. 11 (2019) 22264–22271, https://doi.org/10.1021/acsami.9b03747.

[38] B.H. Toby, EXPGUI, a graphical user interface for GSAS, J. Appl. Crystallogr. 34 (2001) 210–213, https://doi.org/10.1107/S0021889801002242.

[39] R. Hesse, M. Weiss, R. Szargan, P. Streubel, R. Denecke, Improved peak-fit procedure for XPS measurements of inhomogeneous samples-development of the advanced tougaard background method, J. Electron. Spectrosc. 205 (2015) 29–51, https://doi.org/10.1016/j.elspec.2015.06.013.

[40] T.L. Barr, S. Seal, Nature of the use of adventitious carbon as a binding-energy standard, J. Vac. Sci. Technol. A 13 (1995) 1239–1246, https://doi.org/10.1116/1.579868.

[41] C.W. Dong, S.Y. Lu, S.Y. Yao, R. Ge, Z.D. Wang, Z. Wang, P.F. An, Y. Liu, B. Yang, H. Zhang, Colloidal synthesis of ultrathin monoclinic BiVO$_4$ nanosheets for Z-

[42] scheme overall water splitting under visible light, ACS Catal. 8 (2018) 8649–8658, https://doi.org/10.1021/acscatal.8b01645.

[42] R. Abe, M. Higashi, K. Domen, Facile fabrication of an efficient oxynitride TaON photoanode for overall water splitting into H$_2$ and O$_2$ under visible light irradiation, J. Am. Chem. Soc. 132 (2010) 11828–11829, https://doi.org/10.1021/ja1016552.

[43] T. Hisatomi, C. Katayama, Y. Moriya, T. Minegishi, M. Katayama, H. Nishiyama, T. Yamada, K. Domen, Photocatalytic oxygen evolution using BaNbO$_2$N modified with cobalt oxide under photoexcitation up to 740 nm, Energy Environ. Sci. 6 (2013) 3595–3599, https://doi.org/10.1039/C3EE42951B.

[44] T. Yamada, Y. Murata, S. Suzuki, H. Wagata, S. Oishi, K. Teshima, Template-assisted size control of polycrystalline BaNbO$_2$N particles and effects of their characteristics on photocatalytic water oxidation performances, J. Phys. Chem. C 122 (2018) 8037–8044, https://doi.org/10.1021/acs.jpcc.7b12159.

[45] J. Seo, T. Hisatomi, M. Nakabayashi, N. Shibata, T. Minegishi, M. Katayama, K. Domen, Efficient solar-driven water oxidation over perovskite-type BaNbO$_2$N photoanodes absorbing visible light up to 740 nm, Adv. Energy Mater. 8 (2018), 1800094, https://doi.org/10.1002/aenm.201800094.

[46] S.H. Wei, X.X. Xu, Boosting photocatalytic water oxidation reactions over strontium tantalum oxynitride by structural laminations, Appl. Catal. B Environ. 228 (2018) 10–18, https://doi.org/10.1016/j.apcatb.2018.01.071.

[47] Y.W. Wang, S. Jin, G.X. Pan, Z.X. Li, L. Chen, G. Liu, X.X. Xu, Zr doped mesoporous LaTaON$_2$ for efficient photocatalytic water splitting, J. Mater. Chem. A 7 (2019) 5702–5711, https://doi.org/10.1039/C8TA11561C.

[48] L. Yang, J.X. Yu, S.F. Chang, X.X. Xu, Boosting visible-light-driven water splitting over LaTaON$_2$ via Al doping, Sci. China Mater. 65 (2022) 3452–3461, https://doi.org/10.1007/s40843-022-2085-4.

[49] M. Kodera, M. Katayama, T. Hisatomi, T. Minegishi, K. Domen, Effects of flux treatment on morphology of single-crystalline BaNbO$_2$N particles, CrystEngComm 18 (2016) 3186–3190, https://doi.org/10.1039/C5CE02335A.

[50] R. Wang, Q. Wang, J. Qian, X.X. Xu, Visible-light-driven photocatalytic water oxidation over LaNbON$_2$-LaMg$_{2/3}$Nb$_{1/3}$O$_3$ solid solutions, Inorg. Chem. Front. 8 (2021) 2365–2372, https://doi.org/10.1039/D1QI00166C.

[51] S. Balaz, S.H. Porter, P.M. Woodward, L.J. Brinson, Electronic structure of tantalum oxynitride perovskite photocatalysts, Chem. Mater. 25 (2013) 3337–3343, https://doi.org/10.1021/cm401815w.

[52] M.L. Lv, X.Q. Sun, S.H. Wei, C. Shen, Y.L. Mi, X.X. Xu, Ultrathin lanthanum tantalate perovskite nanosheets modified by nitrogen doping for efficient photocatalytic water splitting, ACS Nano 11 (2017) 11441–11448, https://doi.org/10.1021/acsnano.7b06131.

[53] X.X. Xu, R. Wang, X.Q. Sun, M.L. Lv, S. Ni, Layered perovskite compound NaLaTiO$_4$ modified by nitrogen doping as a visible light active photocatalyst for water splitting, ACS Catal. 10 (2020) 9889–9898, https://doi.org/10.1021/acscatal.0c02626.

[54] Y.C. Ko, B.D. Ratner, A.S. Hoffman, Characterization of hydrophilic-hydrophobic polymeric surfaces by contact-angle measurements, J. Coll. Interface Sci. 82 (1981) 25–37, https://doi.org/10.1016/0021-9797(81)90120-X.

[55] J.L. Du, Z.F. Chen, C.C. Chen, T.J. Meyer, A half-reaction alternative to water oxidation: chloride oxidation to chlorine ctalyzed by silver ion, J. Am. Chem. Soc. 137 (2015) 3193–3196, https://doi.org/10.1021/jacs.5b00037.

[56] B.M. Hunter, H.B. Gray, A.M. Muller, Earth-abundant heterogeneous water oxidation catalysts, Chem. Rev. 116 (2016) 14120–14136, https://doi.org/10.1021/acs.chemrev.6b00398.

[57] J.S. Xu, C.S. Pan, T. Takata, K. Domen, Photocatalytic overall water splitting on the perovskite-type transition metal oxynitride CaTaO$_2$N under visible light irradiation, Chem. Commun. 51 (2015) 7191–7194, https://doi.org/10.1039/C5CC01728A.

[58] Y. Pihosh, T. Minegishi, V. Nandal, T. Higashi, M. Katayama, T. Yamada, Y. Sasaki, K. Seki, Y. Suzuki, M. Nakabayashi, M. Sugiyamaa, K. Domen, Ta$_3$N$_5$-nanorods enabling highly efficient water oxidation via advantageous light harvesting and charge collection, Energy Environ. Sci. 13 (2020) 1519–1530, https://doi.org/10.1039/D0EE00220H.

[59] Y.J. Zhong, Z.S. Li, X. Zhao, T. Fang, H.T. Huang, Q.F. Qian, X.F. Chang, P. Wang, S.C. Yan, Z.T. Yu, Z.G. Zou, Enhanced water-splitting performance of perovskite SrTaO$_2$N photoanode film through ameliorating interparticle charge transport, Adv. Funct. Mater. 26 (2016) 7156–7163, https://doi.org/10.1002/adfm.201603021.

[60] S.H. Wei, S.F. Chang, F. Yang, Z.P. Fu, G. Liu, X.X. Xu, Stable and efficient solar-driven photoelectrochemical water splitting into H$_2$ and O$_2$ based on a BaTaO$_2$N photoanode decorated with CoO microflowers, Chem. Commun. 57 (2021) 4412–4415, https://doi.org/10.1039/D0CC07778J.

[61] J.X. Yu, S.F. Chang, L. Shi, X.X. Xu, Single-crystalline Bi$_2$YO$_4$Cl with facet-aided photocarrier separation for robust solar water splitting, ACS Catal. 13 (2023) 3854–3863, https://doi.org/10.1021/acscatal.2c05768.

[62] T.W. Kim, K.S. Choi, Nanoporous BiVO$_4$ photoanodes with dual-layer oxygen evolution catalysts for solar water splitting, Science 343 (2014) 990–994, https://doi.org/10.1126/science.1246913.

[63] H. Xiao, J. Tahir-Kheli, W.A. Goddard, Accurate band gaps for semiconductors from density functional theory, J. Phys. Chem. Lett. 2 (2011) 212–217, https://doi.org/10.1021/jz101565j.

[64] J.H. Yuan, Q. Chen, L.R.C. Fonseca, M. Xu, K.H. Xue, X.S. Miao, GGA-1/2 self-energy correction for accurate band structure calculations: the case of resistive switching oxides, J. Phys. Commun. 2 (2018), 105005, https://doi.org/10.1088/2399-6528/aade7e.

[65] Z. Wang, Y. Luo, T. Hisatomi, J.J.M. Vequizo, S. Suzuki, S.S. Chen, M. Nakabayashi, L.H. Lin, Z.H. Pan, N. Kariya, A. Yamakata, N. Shibata, T. Takata,

K. Teshima, K. Domen, Sequential cocatalyst decoration on BaTaO$_2$N towards highly-active Z-scheme water splitting, Nat. Commun. 12 (2021) 1005, https://doi.org/10.1038/s41467-021-21284-3.